

# Mott-to-Goodenough insulator-insulator transition in $\text{LiVO}_2$

Alaska Subedi

*Centre de Physique Theorique, Ecole Polytechnique, CNRS,  
Université Paris-Saclay, F-91128 Palaiseau, France and  
Collège de France, 11 place Marcelin Berthelot, 75005 Paris, France*  
(Dated: March 2, 2024)

I critically examine Goodenough's explanation for the experimentally observed phase transition in  $\text{LiVO}_2$  using microscopic calculations based on density functional and dynamical mean field theories. The high-temperature rhombohedral phase exhibits both magnetic and dynamical instabilities. Allowing a magnetic solution for the rhombohedral structure does not open an insulating gap, and an explicit treatment of the on-site Coulomb  $U$  interaction is needed to stabilize an insulating rhombohedral phase. The non-spin-polarized phonon dispersions of the rhombohedral phase show two unstable phonon modes at the wave vector  $(\frac{1}{3}, -\frac{1}{3}, 0)$  that corresponds to the experimentally observed trimer forming instability. A full relaxation of the supercell corresponding to this instability yields a nonmagnetic state containing  $\text{V}_3$  trimers. These results are consistent with Goodenough's suggestion that the high-temperature phase is in the localized-electron regime and the transition to the low-temperature phase in the itinerant-electron regime is driven by V-V covalency.

## I. INTRODUCTION

$\text{LiVO}_2$  occurs in a rhombohedral structure with space group  $R\bar{3}m$  above 500 K.<sup>1</sup> In this phase, the  $\text{Li}^+$  and  $\text{V}^{3+}$  cations and  $\text{O}^{2-}$  anions occupy the sites of ordered rocksalt structure, with the -Li-O-V-O- pattern repeating along the rhombohedral [111] direction. This crystallographic arrangement is characterized by alternating Li/V and O layers, where the respective ions make a lattice of equilateral triangles within each layer. Bongers discovered that this material undergoes a first-order structural and magnetic transition around  $T_t \approx 490$  K.<sup>2</sup> The high-temperature phase exhibits a Curie-Weiss magnetic susceptibility. The low-temperature phase does not show any magnetic order and is nonmagnetic. Both phases are insulating.

Several competing explanations have been proposed to explain the phase transition observed in  $\text{LiVO}_2$ . Goodenough has argued that the inplane V-V separation in this material is near a critical distance  $R_c$  that corresponds to the condition where the bandwidth  $W$  is approximately equal to the on-site correlation energy  $U$ .<sup>3</sup> According to his phenomenological theory,<sup>4,5</sup> materials that have V-V distances near  $R_c$  and  $W \approx U$  exhibit an electronic instability that is manifested by the formation of  $\text{V}_3$  trimers below  $T_t$ . In his words, the high-temperature phase is in the localized-electron regime, whereas the low-temperature phase is in the itinerant-electron regime.<sup>5</sup> That is, in the contemporary parlance, the material is a Mott insulator at temperatures  $T > T_t$  and a band insulator when  $T < T_t$ . Each  $\text{V}^{3+}$  ion in  $\text{LiVO}_2$  has two electrons in two  $e_g$  orbitals, which give rise to spin  $S = 1$  per site in the Mott phase. In the low-temperature “Goodenough phase”, the formation of  $\text{V}_3$  trimers results in a gap between the bonding and antibonding molecular orbitals of the trimers. The two electrons per site then completely fill the bonding manifold, with the material displaying a nonmagnetic behavior in this phase.

The trimerization envisaged by Goodenough is differ-

ent from a Peierls distortion. In a Peierls distortion, kinetic energy is gained by moving the occupied electronic states near the Fermi level downwards, and this changes the electronic states only near the Fermi level. By contrast, a Goodenough distortion involves the formation of covalent bonds between neighboring metal ions, and this changes the electronic structure of the whole  $d$  manifold. Furthermore, the Goodenough distortion is also dissimilar to a charge disproportionation because the charge of a V ion is transferred neither to a neighboring V nor O ion.

Pen *et al.* and others have proposed an alternative scenario for the phase transition in  $\text{LiVO}_2$  that involves an orbital ordering of the localized  $\text{V}^{3+} 3d^2$  electrons.<sup>6-9</sup> Since the electrons remain localized in the low-temperature phase, a structural distortion plays a minor role in their picture, and the nature of the insulating gap does not change across the phase transition. The orbital ordering partitions each V layer into three sublattices, and the strong antiferromagnetic exchange between three sites in a triangle leads to the formation of a  $S = 0$  spin-singlet state. This naturally removes the frustration of the antiferromagnetic exchange that is present in the high-temperature phase.

Despite having been first synthesized in 1954, experimental studies on stoichiometric single-crystal  $\text{LiVO}_2$  are relatively scarce because of the difficulty in preparing such samples.<sup>10</sup> Resistivity measurements on polycrystalline samples of this material show an anomaly during the phase transition at  $T_t$ .<sup>11-13</sup> Early x-ray diffraction studies showed that there is a discontinuity in volume around  $T_t$ . However, no change in crystal symmetry across the transition temperature  $T_t$  was found to be apparent.<sup>12,14</sup> Furthermore, weak superlattice peaks that correspond to an enlarged unit cell and are suggestive of a  $\text{V}_3$  trimer formation have also been observed.<sup>15-17</sup> Several independent NMR measurements have confirmed the nonmagnetic nature of the low-temperature phase.<sup>18-20</sup> Pair distribution function analyses of synchrotron data

have additionally found evidence for two different V-V distances below  $T_t$ .<sup>21</sup>

Tian *et al.* were able to grow single crystals of  $\text{LiVO}_2$  in 2004.<sup>22</sup> Their structural, magnetic, and transport studies confirm the first-order paramagnetic-to-nonmagnetic transition in this material. Resistivity measurements show that both phases exhibit activated behavior with small gaps of 0.14 and 0.18 eV in the low- and high-temperature phases, respectively. The small values for the gaps indicate either the presence of Li deficiency or that both phases are in the verge of metallicity. In the latter case, a strongly localized picture may not be appropriate for the two phases. Their electron diffraction experiments also show bright superlattice reflections that are consistent with the trimer model.

The experimental results reviewed above give a consistent picture of an insulator-to-insulator transition from a paramagnetic to a trimerized nonmagnetic state in  $\text{LiVO}_2$  as the temperature is lowered. However, they do not fully clarify whether the borderline localized-itinerant behavior proposed by Goodenough or the strongly localized description of Pen *et al.* is more appropriate for this material, and the debate of whether the covalency or orbital ordering drives the phase transition in this material remains to be settled.

In this paper, I use calculations based on density functional (DFT) and dynamical mean field (DMFT) theories to study the microscopic physics underlying the high- and low-temperature phases of  $\text{LiVO}_2$ . The high-temperature rhombohedral phase exhibits both magnetic and dynamical instabilities. I was able to stabilize ferromagnetic and  $120^\circ$  inplane ordering spin configurations in the rhombohedral structure. However, allowing for a magnetic solution does not open a band gap. A DMFT treatment of the V  $3d$  manifold using reasonable values of the on-site Coulomb  $U$  and Hund's rule coupling  $J_H$  parameters is able to stabilize a paramagnetic insulating state in the rhombohedral structure. The phonon dispersions of the non-spin-polarized rhombohedral phase exhibits two branches that are unstable along extended paths in the Brillouin zone. At the wave vector  $(\frac{1}{3}, -\frac{1}{3}, 0)$ , which corresponds to the trimer forming instability observed in the diffraction experiments, the two modes simultaneously show large imaginary frequencies. I was able to stabilize a trimerized supercell corresponding to this wave vector, and it exhibits an insulating gap. These results reconcile well with Goodenough's suggestion that the high-temperature phase is in the localized-electron regime and the changes in V-V bonding drives a transition to the low-temperature trimerized phase in the itinerant-electron regime.

## II. COMPUTATIONAL DETAILS

The DFT calculations presented here were obtained using the pseudopotential-based planewave method as implemented in the Quantum ESPRESSO package.<sup>23</sup> The

phonon dispersions were calculated using density functional perturbation theory.<sup>24</sup> The cut-offs for the basis-set and charge-density expansions were set to 50 and 500 Ryd, respectively, and a Marzari-Vanderbilt smearing of 0.02 Ryd was used.<sup>25</sup> The calculations were done within the generalized gradient approximation of Perdew, Burke and Ernzerhof<sup>26</sup> using the pseudopotentials generated by Garrity *et al.*<sup>27</sup> I used a  $14 \times 14 \times 14$  grid for Brillouin zone sampling for the rhombohedral cell and equivalent or denser grids for the supercell calculations. The dynamical matrices were calculated on an  $8 \times 8 \times 8$  grid, and the phonon dispersions were obtained by Fourier interpolation. For both the high- and low-temperature phases, the results presented here were calculated using the structures obtained from full relaxation of the lattice parameters in the respective phases without allowing for spin polarization. I also performed some calculations using the general full-potential linearized augmented planewave method as implemented in the WIEN2K package.<sup>28</sup>

The DMFT calculations were performed using tools based on the TRIQS software package developed by Parcollet and Ferrero.<sup>29</sup> The V  $3d$  subspace for the DMFT treatment was constructed from the all-electron electronic structure using the TRIQS/DFTTOOLS package.<sup>30,31</sup> The local Hamiltonian of the V  $3d$  subspace has large off-diagonal elements, and the use of the continuous-time hybridization-expansion Monte Carlo solver TRIQS/CTHYB written by Seth and Krivenko ameliorated the sign problem.<sup>32,33</sup> The calculations were done at an inverse temperature of  $\beta = 23 \text{ eV}^{-1}$  ( $k_B T \simeq 500 \text{ K} > T_t$ ). The spectral functions as a function of energy were obtained by analytically continuing the local Green's function using the maximum entropy method as implemented in the  $\Omega\text{MAXENT}$  code.<sup>34</sup>

## III. RESULTS AND DISCUSSIONS

### A. High-temperature phase

The calculated lattice parameters of the fully-relaxed non-spin-polarized  $\text{LiVO}_2$  in the high-temperature rhombohedral structure are  $a = b = 2.79974$  and  $c = 15.03267$  Å in the hexagonal setting, which agree well with the experimental values.<sup>1</sup> The calculated internal parameter for the O position is  $z_O = 0.24655$ . The band structure of this phase is shown in Fig. 1. It shows a manifold of six bands that lie between  $-8.0$  and  $-3.0$  eV relative to the Fermi energy and have predominantly O  $2p$  character. The five V  $3d$  bands occur between  $-1.5$  and  $3.5$  eV, and the Fermi level corresponds to this manifold being occupied by two electrons.

In the  $\bar{3}m$  point group of the rhombohedral phase, the V  $3d$  orbitals are split into states with one nondegenerate  $a_{1g}$  and two doubly degenerate  $e_g$  irreducible representations. The  $d_{z^2}$  orbital belongs to the  $a_{1g}$  representation, and  $(d_{x^2-y^2}, d_{xy})$  and  $(d_{xz}, d_{yz})$  form two different basis

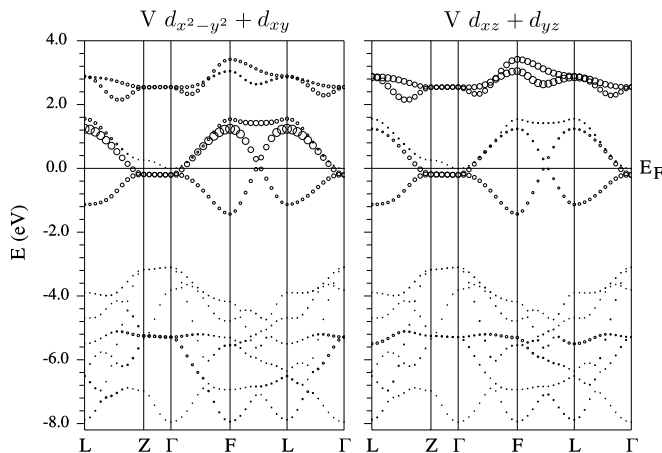


FIG. 1. Calculated non-spin-polarized band structures of rhombohedral  $\text{LiVO}_2$  plotted with circles of size proportional to  $\text{V } d_{x^2-y^2} + d_{xy}$  (left) and  $\text{Ti } d_{xz} + d_{yz}$  (right) characters. The orbitals are defined in the Cartesian coordinates of the conventional unit cell. The band structures are plotted along the path  $L (\frac{1}{2}, 0, 0) \rightarrow Z (\frac{1}{2}, \frac{1}{2}, \frac{1}{2}) \rightarrow \Gamma (0, 0, 0) \rightarrow F (\frac{1}{2}, \frac{1}{2}, 0) \rightarrow L (\frac{1}{2}, 0, 0) \rightarrow \Gamma (0, 0, 0)$  in the Brillouin zone of the primitive unit cell.

TABLE I. The orbital occupations obtained from DFT and DMFT calculations. The DMFT values correspond to the electron densities of the local Green's functions, and the values shown here are for the parameters  $U = 5.5$  and  $J = 0.8$  eV. The negligible asymmetry in the occupations of the degenerate orbitals is due to noise in the calculations.

orbital	DFT	DMFT
$d_{z^2}$	0.570	0.099
$d_{x^2-y^2}$	0.428	0.554
$d_{xy}$	0.428	0.555
$d_{yz}$	0.287	0.394
$d_{xz}$	0.287	0.396

for the  $e_g$  representation. In the electronic structure of  $\text{LiVO}_2$ , the higher-lying two V 3d bands have a mostly  $d_{xz} + d_{yz}$  character and are separated from a manifold of lower-lying three bands. These three V 3d bands are derived from a pair of bands that show a mainly  $d_{x^2-y^2} + d_{xy}$  character and a band that has a dominant  $d_{z^2}$  character. As the band characters depicted in Fig. 1 show, there is considerable mixing of orbital characters between the two sets of  $e_g$  bands. This mixing is also evident from the orbital occupations calculated using local projectors,<sup>30</sup> as shown in Table I. The  $d_{xz}$  and  $d_{yz}$  orbitals that are nominally unoccupied each contain almost 0.3 electrons, and this is due to the covalency with the  $d_{x^2-y^2}$  and  $d_{xy}$  orbitals. Furthermore, I find that the three bands in the lower V 3d manifold show intermixing of  $d_{z^2}$  and  $d_{x^2-y^2} + d_{xy}$  characters. In fact, there is substantial  $d_{z^2}$  character (not shown) in the occupied part of the nominal  $e_g$  band, which accounts for the fact that the  $d_{z^2}$  orbital has the largest occupancy with almost 0.6 electrons.

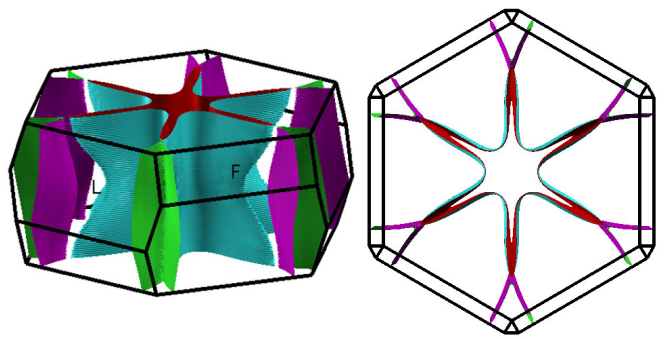


FIG. 2. (Color online) Calculated non-spin-polarized Fermi surface of rhombohedral  $\text{LiVO}_2$ . The left and right panels show two different views of the same Fermi surface.

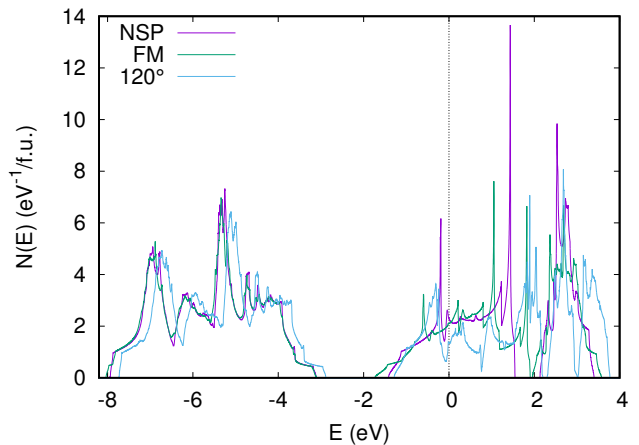


FIG. 3. (Color online) Calculated DOS of rhombohedral  $\text{LiVO}_2$  in the non-spin-polarized, ferromagnetic and  $120^\circ$  ordered configurations.

The Fermi surface of non-spin-polarized  $\text{LiVO}_2$  in the high-temperature rhombohedral structure, shown in Fig. 2, is rather three-dimensional. The Fermi surface does not exhibit any obvious nesting. However, the Fermi level is situated at a place with high density of states (DOS), as depicted in Fig. 3. The calculated DOS at the Fermi level is  $N(E_F) = 2.3 \text{ eV}^{-1}$  on a per formula unit both spin basis. Using a value for the Stoner parameter of  $I = 0.8$ , one gets  $NI/2 > 1$ , which puts this material in the regime of ferromagnetic instability. I was able to stabilize both the ferromagnetic and the  $120^\circ$  inplane ordering configurations of spins. The  $120^\circ$  ordered phase is 100 meV per V lower in energy compared to the ferromagnetic state, which itself is only 6 meV per V lower than the non-spin-polarized state. This indicates the presence of a strong antiferromagnetic interaction, especially considering the relatively small values of 0.56 and  $1.02 \mu_B$  for the calculated spin moments on the V sites in the ferromagnetic and  $120^\circ$  ordered phase, respectively. The calculated spin moments are strongly reduced from the value of  $2 \mu_B$  expected for the  $S = 1$  spins due to localized  $\text{V}^{3+}$  ( $d^2$ ) electrons. This reduction of moments is at odds

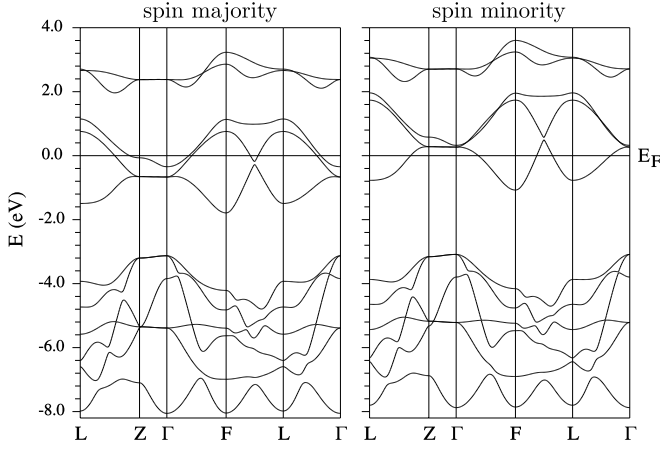


FIG. 4. Calculated spin majority (left) and spin minority (right) band structures of rhombohedral  $\text{LiVO}_2$  in the ferromagnetic state.

with the results of magnetic susceptibility measurements that show the effective moment to have a value  $\mu_{\text{eff}} \approx 3.3 \mu_B$ ,<sup>12,22</sup> which is close to the value of  $\mu_{\text{eff}} = 2.8 \mu_B$  due to a localized  $S = 1$  moment. This disagreement suggests that the itinerant picture of magnetism given by DFT may not be adequate to describe the high-temperature phase of  $\text{LiVO}_2$ .

The calculated DOS at the Fermi energy gets reduced when a magnetic solution is allowed (see Fig. 3). However, an insulating gap does not materialize in either spin configuration, again in contrast to the resistivity measurements that show an activated behavior.<sup>12,22</sup> I examined the band structure of the ferromagnetic state, shown in Fig. 4, to check if the metallic state obtained from DFT calculations is due to an underestimation of the band gap. In the spin majority sector, the Fermi level passes through two bands. It crosses the upper part of one nominally  $e_g$  band and also goes through the lower part of the nominally  $a_g$  band. In the spin minority sector, the Fermi level crosses the lower section of one nominally  $e_g$  band. However, increasing the exchange splitting and making the  $e_g$  manifold fully unoccupied in the spin-minority sector will not make the material insulating because the Fermi level would still cross the partially occupied  $a_g$  band. To obtain an insulating gap, the partially occupied  $a_g$  band should be shifted above the Fermi level. Even in the  $120^\circ$  ordered spin configuration, I find that the Fermi level crosses through the  $a_g$  band. Therefore, it seems necessary to explicitly take into account the effects of the onsite Coulomb repulsion  $U$ , which will unfill the less-than-half-filled  $a_g$  band. Indeed, a DFT+ $U$  study on a related material  $\text{NaVO}_2$  has found an insulating state when the  $a_g$  band is completely empty.<sup>35</sup>

I performed DMFT calculations on the whole V  $3d$  manifold to confirm the above-described picture of the high-temperature insulating phase of  $\text{LiVO}_2$ . It is necessary to treat all the V  $3d$  orbitals within DMFT even

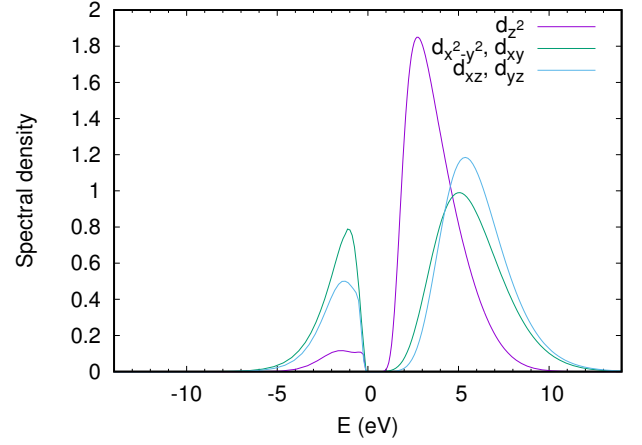


FIG. 5. (Color online) Momentum-integrated spectral functions (local DOS) of paramagnetic  $\text{LiVO}_2$  in the high-temperature rhombohedral structure, as obtained from DMFT calculations using  $U = 5.5$  and  $J_H = 0.8$  eV. The spectra were obtained by analytic continuation of the local Green's function in the imaginary Matsubara frequencies to real frequency using the maximum entropy method.

though the lower  $e_g$  and the  $a_g$  manifold are completely separated from the upper  $e_g$  manifold because the orbital characters of the two  $e_g$  manifolds are substantially mixed. A calculation that only considers the lower three bands would in effect be neglecting the offdiagonal parts of the local Hamiltonian and would not realistically describe the electronic interactions present in the material.

I used  $J_H = 0.8$  eV and a range of values between 4 and 6 eV for  $U$  ( $= F^0$ ) for the onsite interactions in my DMFT calculations. I could only obtain a paramagnetic insulating solution for  $U > 5$  eV. The existence of the insulating solution seems to be contingent upon a low occupancy of the  $d_{z^2}$  (*i.e.*, the  $a_g$ ) orbital. When  $U < 5$  eV, the occupancy of the  $d_{z^2}$  orbital is large (albeit reduced from the DFT value), and the system is metallic because the  $d_{z^2}$  state shows a finite spectral weight at the Fermi level.

The momentum integrated spectral function for the case of  $U = 5.5$  and  $J_H = 0.8$  eV is shown in Fig. 5 to illustrate the electronic structure of the high-temperature paramagnetic Mott insulating phase. The spectra display lower and upper Hubbard bands, which correspond to the removal and addition of an electron, respectively. The spectral weight of the  $d_{z^2}$  orbital below the gap is very small, consistent with the above discussion. The peak of the  $d_{z^2}$  spectral function lies below the peak of the upper Hubbard band. So the insulating state is characterized by a gap between the lower Hubbard band and the unoccupied  $d_{z^2}$  band rather than the Mott-Hubbard gap. The  $d_{x^2-y^2}$  and  $d_{xy}$  orbitals, which belong to the lower  $e_g$  manifold, show larger spectral weight below the gap. In addition, the  $d_{xz}$  and  $d_{yz}$  orbitals also show sizable weight in the lower Hubbard band. This shows that the orbitals belonging to both the  $e_g$  manifolds remain

partially occupied in the insulating state.

The paramagnetic insulating state obtained from DMFT calculations is qualitatively consistent with Goodenough's suggestion that the high-temperature phase of  $\text{LiVO}_2$  is in the localized-electron regime. The calculated spectral functions and the orbital occupancies summarized in Table I give a quantitative description of this Mott phase, and it would be interesting to perform spectroscopy experiments to see if these calculations realistically describe its electronic structure.

### B. Low-temperature phase

As mentioned above,  $\text{LiVO}_2$  undergoes a first-order structural phase transition from a paramagnetic insulating to a nonmagnetic insulating phase below 490 K. The signatures of the structural transition are seen in the x-ray and electron diffraction experiments that indicate a tripling of the unit cell. The crystal structure of the low-temperature phase has not been fully determined. However, Goodenough has suggested that the low-temperature phase is characterized by the formation of  $\text{V}_3$  trimers,<sup>3</sup> and recent pair distribution function analyses show the presence of two distinct V-V distances in the low-temperature phase.<sup>21</sup> It is not known whether the positions of Li and O ions also change during the phase transition.

I calculated the phonon dispersions of the non-spin-polarized high-temperature rhombohedral phase to investigate if it shows any structural instabilities. As can be seen in Fig. 6, the phonon dispersions show two branches that are unstable along extended paths in the Brillouin zone. These branches are connected to the two acoustic modes near the zone center that are polarized in the inplane direction. An inspection of the eigenvectors of these unstable modes shows that the instability involves large inplane displacement of V ions. Additionally, the components of these eigenvectors that correspond to Li and O ions also show finite values, but they are smaller than the V component. Unlike the V displacement, the Li and O components are mostly polarized in the out-of-plane direction.

The displacement patterns of the two unstable modes differ mainly in two aspects. First, the inplane V displacements due to these two unstable modes are in orthogonal directions. Second, the two O ions in the primitive unit cell move in the opposite directions along the  $z$  axis for one mode, while they move in the same direction along the  $z$  axis for the other mode. The eigenvectors of the two unstable modes at the vector  $(\frac{1}{3}, -\frac{1}{3}, 0)$  with respect to the reciprocal lattice vectors of the primitive unit cell are shown in Table II, and they exemplify the above-discussed characteristics of the unstable modes at other points in the Brillouin zone as well.

The point  $(\frac{1}{3}, -\frac{1}{3}, 0)$  in the Brillouin zone corresponds to the volume tripling instability that causes the phase transition in  $\text{LiVO}_2$ . Thus, the calculations of the phonon

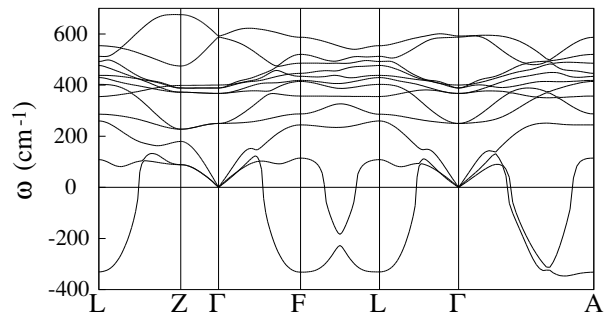


FIG. 6. Calculated phonon dispersions of non-spin-polarized  $\text{LiVO}_2$  in the high-temperature rhombohedral structure. The point  $A$  is  $(\frac{1}{2}, -\frac{1}{2}, 0)$ . The imaginary frequencies are represented with negative values.

TABLE II. The eigendisplacement vectors of the two unstable phonon modes of non-spin-polarized  $\text{LiVO}_2$  in the rhombohedral structure at the wavevector  $(\frac{1}{3}, -\frac{1}{3}, 0)$ .

atom	$x$	$y$	$z$
$\omega = 337i \text{ cm}^{-1}$			
Li	$0.002 + 0.000i$	$0.000 + 0.000$	$-0.144 + 0.000i$
V	$-0.799 + 0.000i$	$0.000 + 0.000$	$-0.003 + 0.000i$
O	$-0.019 + 0.000i$	$0.000 - 0.040$	$0.410 + 0.000i$
O	$-0.019 + 0.000i$	$0.000 + 0.040$	$0.410 + 0.000i$
$\omega = 334i \text{ cm}^{-1}$			
Li	$0.000 + 0.000i$	$0.000 - 0.004i$	$0.000 + 0.000i$
V	$0.000 + 0.000i$	$0.000 - 0.807i$	$0.000 + 0.000i$
O	$0.017 + 0.000i$	$0.000 + 0.038i$	$0.415 + 0.000i$
O	$-0.017 + 0.000i$	$0.000 + 0.038i$	$-0.415 + 0.000i$

dispersions show that low-temperature phase is stabilized by the condensation of two unstable phonons. A symmetry analysis of the two unstable modes shows that they belong to the irreducible representation  $A'$  of the point group  $m$ . Therefore, the low-temperature structure should have the point group  $m$ , which has less symmetry than the point group  $\bar{3}m$  of the high-temperature phase. Structures belonging to the  $m$  crystal class lack inversion symmetry, and the low-symmetry structure resulting from these phonon instabilities should be polar.

I performed a full relaxation of a 36-atom unit cell to study the structural distortions caused by the two unstable phonons identified above. The fully-relaxed structure was refined using the SPGLIB code,<sup>36</sup> which resolved a primitive unit cell with three formula units (12 atoms). The structure could also be refined to a primitive cell with two formula units when the FINDSYM code<sup>37</sup> was used. The space group of the relaxed structure is  $Cm$  (no. 8), and this structure indeed does not have an inversion symmetry, as expected from the discussion above.

The full structural information of the relaxed structure is given in Table III. This structure is graphically depicted in Fig. 7, and one can see that it exhibits the  $\text{V}_3$  trimers predicted by Goodenough for the low-

temperature phase. The calculated DOS for this structure, shown in Fig. 8, displays a band gap of 0.78 eV, which is larger than the experimental value of 0.14 eV obtained from transport measurements.<sup>22</sup> I did not find any magnetic instabilities in this phase. The calculated total energy of this phase is 244 and 138 meV per formula unit lower than the non-spin-polarized and the 120° ordered high-temperature rhombohedral phases, respectively. Therefore, this structure likely represents the low-temperature trimerized phase proposed by Goodenough. The DOS of both O 2*p* and V 3*d* manifolds in the trimerized phase differ drastically from that of the high-temperature phase. In particular, the V 3*d* manifold gets separated into different clusters, which indicates that the V-V bonding is different in the trimerized phase. This is in contrast to the Peierls-type instability that only modifies the electronic structure near the Fermi surface. The changes in the V-V bonding that underlies the instability towards the V<sub>3</sub> trimer formation and the resulting modification of the electronic structure over a large energy scale is a hallmark of a Goodenough transition.

LiVO<sub>2</sub> is not the only material to show a finite wave vector instability due to a local bonding instability. Similar mechanism has been discussed for IrTe<sub>2</sub> and NbSe<sub>2</sub>.<sup>38–40</sup> However, the calculated changes in the electronic structure of these two materials are not as dramatic as in LiVO<sub>2</sub>.

The microscopic calculations presented here allow me to further explore the details of the low-temperature Goodenough phase. I find that the V<sub>3</sub> trimers do not form equilateral triangles. Two V-V distances within the trimer are equal to 2.43 Å, whereas the third V-V distance is 2.44 Å. This distortion of the V<sub>3</sub> trimer is small, but it is not negligible. Within the larger V<sub>3</sub> triangle, all V-V distances are different, with values of 3.01, 3.02 and 3.03 Å. For comparison, I find V-V distance in the high-temperature rhombohedral structure to be 2.80 Å. In addition, the Li-Li distances also change, but these changes are much smaller. There is a smaller Li<sub>3</sub> tri-

TABLE III. Atomic positions of the fully-relaxed trimerized LiVO<sub>2</sub>. The lattice parameters are  $a = b = 4.86962$ ,  $c = 5.26480$  Å,  $\alpha = \beta = 98.87633^\circ$ , and  $\gamma = 119.94979^\circ$ , and the space group is  $Cm$ .

atom	$x$	$y$	$z$
Li	0.01430	0.01430	0.02264
Li	0.32383	0.66314	0.00237
Li	0.66314	0.32383	0.00237
V	0.11709	0.82778	0.50433
V	0.54164	0.54164	0.50611
V	0.82778	0.11709	0.50433
O	0.57274	0.90918	0.74189
O	0.90918	0.57274	0.74189
O	0.24133	0.24133	0.74160
O	0.42252	0.08987	0.28662
O	0.73706	0.73706	0.23030
O	0.08987	0.42252	0.28662

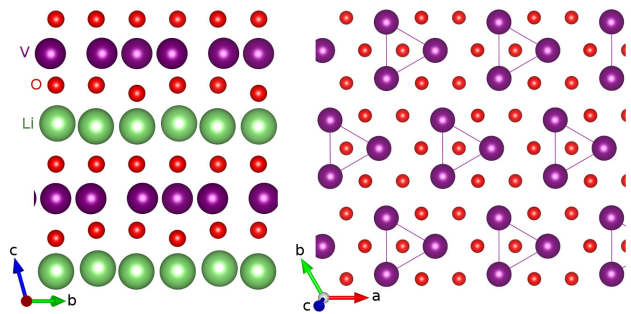


FIG. 7. (Color online) The trimerized phase of LiVO<sub>2</sub> as obtained from structural relaxations described in the text. The left panel shows the layering, while the right panel shows a single VO<sub>2</sub> layer. The V<sub>3</sub> trimers are indicated by solid lines. The large green, medium violet, and small red spheres denote Li, V, and O ions, respectively.

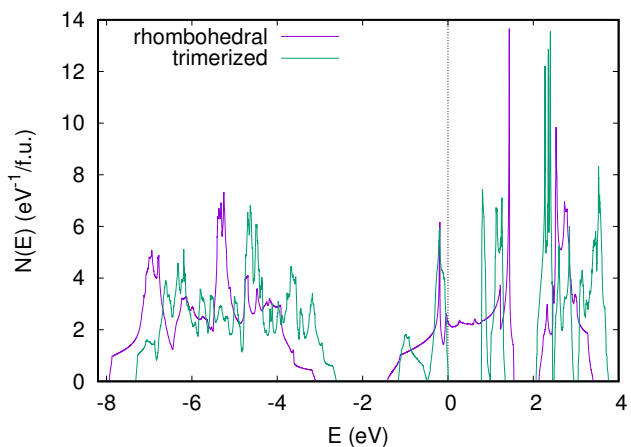


FIG. 8. (Color online) Calculated non-spin-polarized DOS in LiVO<sub>2</sub> in the rhombohedral and trimerized structures.

angle with two Li-Li distances of 2.79 Å and one Li-Li distance of 2.77 Å, and a larger Li<sub>3</sub> triangle with two Li-Li distances of 2.89 Å and one Li-Li distance of 2.86 Å.

Although the V-V distances change substantially as a result of the trimer formation, I find less than 1% difference in volume per formula unit between the two phases, again in agreement with the experimental observation.<sup>13</sup> The VO<sub>6</sub> and LiO<sub>6</sub> octahedra keep their structural integrity and show only modest changes in the low-temperature phase. The volume of the VO<sub>6</sub> octahedron in the high-temperature phase is 10.87 Å<sup>3</sup>. In the low-temperature phase, the primitive unit cell has one VO<sub>6</sub> octahedron with a volume of 10.87 Å<sup>3</sup> and two VO<sub>6</sub> octahedra with a volume of 10.82 Å<sup>3</sup>. Similarly, the volume of the LiO<sub>6</sub> octahedron in the high-temperature phase is 11.81 Å<sup>3</sup>. In the low-temperature phase, there is one LiO<sub>6</sub> octahedron with a volume of 12.08 Å<sup>3</sup> and two more with a volume of 12.00 Å<sup>3</sup>.

The Li and V ions are displaced from the center of their octahedral cage within the *ab* plane in the low-

temperature phase. But this does not generate a large remnant electric dipole because the formation of trimers cancels out the dipole moment on average. Nevertheless, the Li layer and one O layer are buckled in the out-of-plane direction. [The other O layer is flat.] A pair each of Li and O ions are buckled in one direction while the third Li and O ions are displaced in the opposite direction (see Fig. 7). Unlike the dipole moments due to the offcenterings of Li and V ions within the  $ab$  plane, the dipole moments arising from the uneven buckling of the Li and O layers do not cancel out on average. Therefore, the low-temperature phase of  $\text{LiVO}_2$  should show a finite electric polarization. However, it will likely be difficult to change the O-O distances necessary to switch the polarization, and this material cannot probably be characterized as a ferroelectric.

#### IV. SUMMARY AND CONCLUSIONS

In summary, I have used microscopic calculations based on DFT and DMFT to critically examine Goodenough's explanation for the experimentally observed insulator-to-insulator phase transition in  $\text{LiVO}_2$ . I find that the high-temperature rhombohedral phase exhibits both magnetic and dynamical instabilities. The rhombohedral phase does not display an insulating gap when

a magnetic solution is allowed because the spin-majority bands are always partially occupied within DFT. I was able to obtain an insulating paramagnetic solution with reasonable values of the onsite Coulomb  $U$  and Hund's rule coupling  $J_H$  parameters using DMFT calculations. The non-spin-polarized phonon dispersions of the rhombohedral phase show large instabilities of two modes at the wave vector  $(\frac{1}{3}, -\frac{1}{3}, 0)$ , which corresponds to the extra peaks observed in the diffraction experiments below the phase transition. A full relaxation of the supercell corresponding to this instability resulted in a nonmagnetic phase that contains  $\text{V}_3$  trimers. In addition, the Li and O ions are also displaced due to this structural instability. These results support Goodenough's suggestion that the high-temperature phase of  $\text{LiVO}_2$  is in the localized-electron regime and the V-V covalency drives the transition to a low-temperature trimerized phase in the itinerant-electron regime.

#### ACKNOWLEDGMENTS

This work was supported by the European Research Council grants ERC-319286 QMAC and ERC-61719 CORRELMAT and the Swiss National Supercomputing Center (CSCS) under project s575.

- 
- <sup>1</sup> W. Rüdorff and H. Becker, Z. Naturforsch. **9B**, 613 (1954).
  - <sup>2</sup> P. F. Bongers, Ph.D. thesis, The University of Leiden, Leiden, The Netherlands (1957).
  - <sup>3</sup> J. B. Goodenough, *Magnetism and the Chemical Bond* (Interscience, New York, 1963).
  - <sup>4</sup> J. B. Goodenough, Phys. Rev. **120**, 67 (1960).
  - <sup>5</sup> J. B. Goodenough, G. Dutta and A. Manthiram, Phys. Rev. B **43**, 10170 (1991).
  - <sup>6</sup> H. F. Pen, J. van den Brink, D. I. Khomskii, and G. A. Sawatzky, Phys. Rev. Lett. **78**, 1323 (1997).
  - <sup>7</sup> H. F. Pen, L. H. Tjeng, E. Pellegrin, F. M. F. de Groot, G. A. Sawatzky, M. A. van Veenendaal, and C. T. Chen, Phys. Rev. B **55**, 15500 (1997).
  - <sup>8</sup> S. Y. Ezhov, V. I. Anisimov, H. F. Pen, D. I. Khomskii, and G. A. Sawatzky, Europhys. Lett. **44**, 491 (1998).
  - <sup>9</sup> J. Yoshitake and Y. Motome, J. Phys. Soc. Jpn. **80**, 073711 (2011).
  - <sup>10</sup> T. A. Hewston and B. L. Chamberland, J. Solid State Chem. **59**, 168 (1985).
  - <sup>11</sup> B. Reuter, R. Weber, and J. Jaskowski, Z. Elektrochem. **66**, 832 (1962).
  - <sup>12</sup> K. Kobayashi, K. Kosuge, and S. Kachi, Mat. Res. Bull. **4**, 95 (1969).
  - <sup>13</sup> T. A. Hewston and B. L. Chamberland, J. Solid State Chem. **65**, 100 (1986).
  - <sup>14</sup> P. F. Bongers, in *Crystal Structure and Chemical Bonding in Inorganic Chemistry*, edited by C. J. M. Rooymans and A. Rabenau (Elsevier, New York, 1975), Chap. 4.
  - <sup>15</sup> M. Onoda and T. Inabe, J. Phys. Soc. Jpn. **62**, 2216 (1993).
  - <sup>16</sup> K. Takao and M. Onoda, J. Phys.: Condens. Matter **22**, 116003 (2010).
  - <sup>17</sup> J. M. Gaudet and J. R. Dahn, Can. J. Phys. **91**, 444 (2013).
  - <sup>18</sup> M. Onoda, T. Naka, and H. Nagasawa, J. Phys. Soc. Jpn. **60**, 2550 (1991).
  - <sup>19</sup> J. Kikuchi, S. Kambe, H. Yasuoka, Y. Ueda, K. Tomimoto, and J. Akimitsu, J. Phys. Soc. Jpn. **60**, 3620 (1991).
  - <sup>20</sup> T. Jin-no, Y. Shimizu, M. Itoh, S. Niitaka, and H. Takagi, Phys. Rev. B **87**, 075135 (2013).
  - <sup>21</sup> F. Pourpoint, X. Hua, D. S. Middlemiss, P. Adamson, D. Wang, P. G. Bruce, and C. P. Grey, Chem. Mater. **24**, 2880 (2012).
  - <sup>22</sup> W. Tian, M. F. Chisholm, P. G. Khalifah, R. Jin, B. C. Sales, S. E. Nagler, and D. Mandrus, Mater. Res. Bull. **39**, 1319 (2004).
  - <sup>23</sup> P. Giannozzi, S. Baroni, N. Bonini, M. Calandra, R. Car, C. Cavazzoni, D. Ceresoli, G. L. Chiarotti, M. Cococcioni, I. Dabo *et al.*, J. Phys.: Condens. Matter **21**, 395502 (2009).
  - <sup>24</sup> S. Baroni, S. de Gironcoli, A. Dal Corso, and P. Giannozzi, Rev. Mod. Phys. **73**, 515 (2001).
  - <sup>25</sup> N. Marzari, D. Vanderbilt, A. De Vita, and M. C. Payne, Phys. Rev. Lett. **82**, 3296 (1999).
  - <sup>26</sup> J. P. Perdew, K. Burke, and M. Ernzerhof, Phys. Rev. Lett. **77**, 3865 (1996).
  - <sup>27</sup> K. F. Garrity, J. W. Bennett, K. M. Rabe, and D. Vanderbilt, Comp. Mater. Sci. **81**, 446 (2014).
  - <sup>28</sup> P. Blaha, K. Schwarz, G. Madsen, D. Kvasnicka, and J. Luitz, "WIEN2k, An Augmented Plane Wave + Local Orbitals Program for Calculating Crystal Properties" (K.

- Schwarz, Tech. Univ. Wien, Austria) (2001).
- <sup>29</sup> O. Parcollet, M. Ferrero, T. Ayrat, H. Hafermann, I. Krivenko, L. Messio, and P. Seth, *Comp. Phys. Comm.* **196**, 398 (2015).
  - <sup>30</sup> M. Aichhorn, L. Pourovskii, V. Vildosola, M. Ferrero, O. Parcollet, T. Miyake, A. Georges, and S. Biermann, *Phys. Rev. B* **80**, 085101 (2009).
  - <sup>31</sup> M. Aichhorn, L. Pourovskii, P. Seth, V. Vildosola, M. Zingl, O. E. Peil, X. Deng, J. Marvlje, G. Kraberger, C. Martins, M. Ferrero, and O. Parcollet, *Comm. Phys. Commun.* **204**, 200 (2016).
  - <sup>32</sup> E. Gull, A. J. Millis, A. I. Lichtenstein, A. N. Rubtsov, M. Troyer, and P. Werner, *Rev. Mod. Phys.* **83**, 349 (2011).
  - <sup>33</sup> P. Seth, I. Krivenko, M. Ferrero, and O. Parcollet, *Comp. Phys. Comm.* **200**, 274 (2016).
  - <sup>34</sup> D. Bergeron and A.-M. S. Tremblay, *Phys. Rev. E* **94**, 023303 (2016).
  - <sup>35</sup> T. Jia, G. Zhang, Z. Zeng, and H. Q. Lin, *Phys. Rev. B* **80**, 045103 (2009).
  - <sup>36</sup> A. Togo, SPGLIB, a C library for finding and handling crystal symmetries, <https://atztogo.github.io/spglib/>.
  - <sup>37</sup> H. T. Stokes and D. M. Hatch, *J. Appl. Cryst.* **38**, 237-238 (2005).
  - <sup>38</sup> A. F. Fang, G. Xu, T. Dong, P. Zheng, and N. L. Wang, *Nat. Sci. Rep.* **3**, 1153 (2013).
  - <sup>39</sup> H. Cao, B. C. Chakoumakos, X. Chen, J. Yan, M. A. McGuire, H. Yang, R. Custelcean, H. Zhou, D. J. Singh, and D. Mandrus, *Phys. Rev. B* **88**, 115122 (2013).
  - <sup>40</sup> M. Calandra, I. I. Mazin, and F. Mauri, *Phys. Rev. B* **80**, 241108(R) (2009).